

# 3D-Printing Damage-Tolerant Architected Metallic Materials with Shape Recoverability via Special Deformation Design of Constituent Material

Zhiwei Xiong,<sup>◆</sup> Meng Li,<sup>◆</sup> Shijie Hao,\* Yinong Liu, Lishan Cui, Hong Yang,\* Chengbo Cui, Daqiang Jiang, Ying Yang,\* Hongshuai Lei, Yihui Zhang, Yang Ren, Xiaoyu Zhang, and Ju Li

Cite This: *ACS Appl. Mater. Interfaces* 2021, 13, 39915–39924

Read Online

ACCESS |

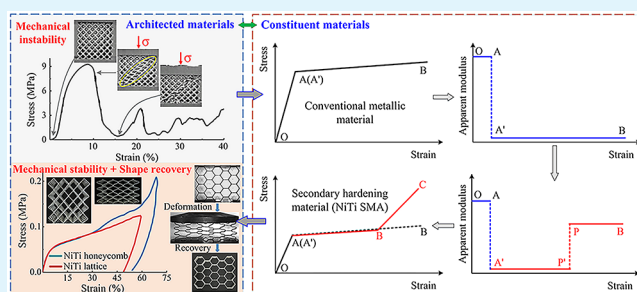
Metrics & More

Article Recommendations

Supporting Information

**ABSTRACT:** Architected metallic materials generally suffer from a serious engineering problem of mechanical instability manifested as the emergence of localized deformation bands and collapse of strength. They usually cannot exhibit satisfactory shape recoverability due to the little recoverable strain of metallic constituent material. After yielding, the metallic constituent material usually exhibits a continuous low strain-hardening capacity, giving the local yielded regions of architecture low load resistance and easily developing into excessive deformation bands, accompanied by the collapse of strength. Here, a novel constituent material deformation design strategy has been skillfully proposed, where the low load resistance of yielded regions of the architecture can be effectively compensated by the significant self-strengthening behavior of constituent material, thus avoiding the formation of localized deformation bands and collapse of strength. To substantiate this strategy, shape-memory alloys (SMAs) are considered as suitable constituent materials for possessing both self-strengthening behavior and shape-recovery function. A 3D-printing technique was adopted to prepare various NiTi SMA architected materials with different geometric structures. It is demonstrated that all of these architected metallic materials can be stably and uniformly compressed by up to 80% without the formation of localized bands, collapse of strength, and structural failure, exhibiting ultrahigh damage tolerance. Furthermore, these SMA architected materials can display more than 98% shape recovery even after 80% deformation and excellent cycle stability during 15 cycles. This work exploits the amazing impact of constituent materials on constructing supernormal properties of architected materials and will open new avenues for developing high-performance architected metallic materials.

**KEYWORDS:** 3D printing, architected metallic materials, shape-memory alloys, damage-tolerant, shape recoverability



## 1. INTRODUCTION

Architected metallic materials refer to materials with specifically designed geometries to achieve enhanced mechanical performance;<sup>1</sup> they can be monolithic materials, such as I-beams, or complex structures with periodic arrangements of identical unit cells, such as honeycomb boards.<sup>2</sup> These materials offer a unique advantage that allows us to combine the desirable characteristics of geometrical structures and the intrinsic properties of constituent materials, thus providing the ability to improve or reach new mechanical performance levels not achievable with bulk materials.<sup>3,4</sup> Illustrative examples may include helical springs that can magnify the elastic stretch of a material by a factor of 1000, metallic microlattices that have very low mass and high specific strength,<sup>5</sup> and structures that exhibit lateral expansion when pulled in one direction, e.g., negative Poisson ratio materials.<sup>6</sup> The recent advances in 3D-printing technology have propelled the research and develop-

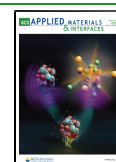
ment of architected metallic materials with novel properties to a new height.<sup>2,7–11</sup>

However, architected metallic materials usually suffer from a universal weakness in load-bearing applications. In such architectures, the load distribution is naturally inhomogeneous, and failure due to local plastic deformation initiates at sites with the highest load-to-strength ratios. In addition, the local deformation often causes shape or orientation changes in the members of the architecture in a way that weakens the load-bearing capacity of the structure, i.e., structural weakening.<sup>12,13</sup> This process leads to the formation of localized deformation

Received: June 16, 2021

Accepted: August 5, 2021

Published: August 16, 2021



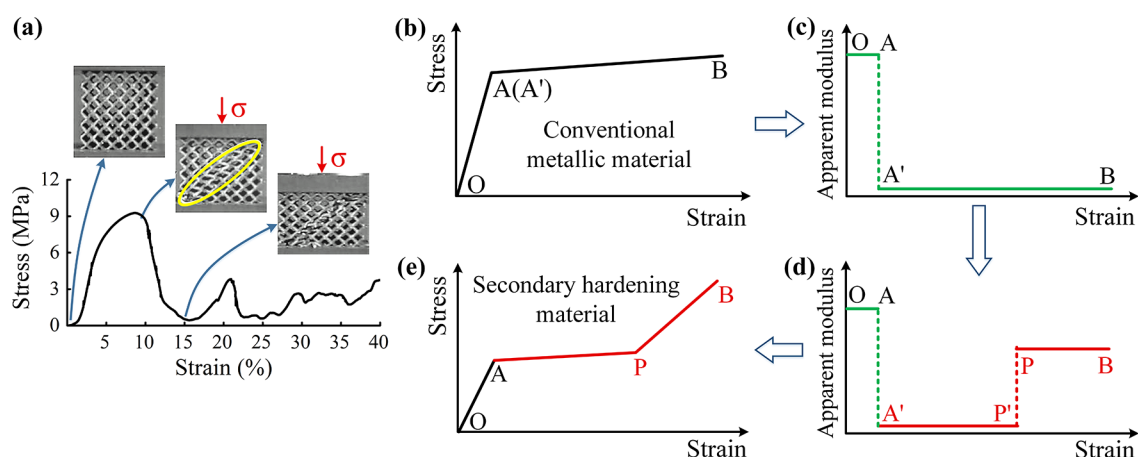


**Figure 1.** Structural instability phenomenon and schematics of the deformation design of constituent material for damage-tolerant architected metallic materials. (a) Stress–strain behavior and formation of a localized deformation band in a metallic lattice structure. Images reprinted with permission from ref 14. Copyright 2016 Elsevier. (b) Schematic of the stress–strain behavior of a conventional metallic material, which presents a continuous plastic deformation with low hardening capacity after yielding. Point A (A′) represents the yielding point. (c) Schematic of the tangent modulus as a function of strain of the conventional metallic material. (d) Schematic of the apparent modulus as a function of strain of the specially designed constituent material. Stage PB represents the introduced high apparent modulus deformation stage. (e) Corresponding stress–strain curve of the constituent material in (d), which is called the secondary hardening material.

bands of excessively high strain or local fracture, thus causing the catastrophic destruction of the architecture and collapse of strength. Figure 1a shows the compression stress–strain curve of a 3D-printed metallic lattice structure and illustrates the significant loss of the load-bearing capacity (weakening) of the structure after initial yielding and the formation of a localized deformation band of high local strain.<sup>14</sup> This process represents a typical issue of mechanical instability, which brings severe uncontrollability and unpredictability in practical applications. Besides, because of the small recoverable strain of the metallic material, most architected metallic materials cannot exhibit satisfactory shape recoverability after deformation, especially large deformation. This causes architected metallic materials to be single use only and a huge resource waste.

A general perception of the localized deformation bands emerging in architected metallic materials is ascribed to the structural factor such as geometric imperfection or singly oriented arrangements of unit cells.<sup>4,13</sup> Hence, structure designs are commonly adopted such as shell-like mesostructures or crystal-inspired mesoscale structures.<sup>4,15</sup> Although these structural designs can improve the damage-tolerance of architected materials, local structural collapses and strength loss still exist and the local deformation bands do not get completely eliminated. Besides, pure structural design cannot satisfy the requirements of high shape recoverability and high cycling stability of architected metallic materials in practical engineering applications.

When an architected metallic material is loaded in a uniaxial manner, the stress concentration will appear along the maximum shearing stress plane, which is a mechanical phenomenon and is unavoidable. This stress concentration will cause the shearing plane preferential deformation and induce the initiation of local bands when loaded beyond the yield point.<sup>12</sup> As is known, a conventional elastic-plastic metallic material usually exhibits a low strain-hardening capacity (low apparent modulus) after yielding (A(A′)–B in Figure 1b and c), thus causing the stiffness decrease of the architected material and the sudden loss of mechanical

strength. With the increase of load, this low apparent modulus issue continues until the fracture (A′–B in Figure 1c), making the local bands keep evolving into collapse until their cell walls come into contact or fracture failure, accompanied by local excessive deformation and high strain concentration.

It is apparent that the persistent low apparent modulus of the constituent material after yielding is mainly responsible for the bad evolution of the local bands in the architected metallic materials. Hence, a possible method to prevent the local bands from generating into excessive deformation is blocking the continuous development of low modulus deformation by introducing a high modulus deformation stage behind it (P–B in Figure 1d). This high modulus deformation stage can significantly enhance the load resistance of the preferentially yielded regions (local bands) and facilitate deformation spreading to other regions, thus effectively inhibiting excessive deformation of the local bands. This material deformation design strategy aims to compensate for the loss of structural stiffness with the significant self-strengthening behavior of the constituent material. Figure 1e shows the schematics of the corresponding stress–strain behaviors of such constituent materials, called secondary hardening materials. In this deformation behavior, the low modulus deformation stage with a finite and suitable strain span (A–P in Figure 1e) can provide enough deformation capacity for the whole architected material without fracture, and the following high modulus deformation stage (P–B in Figure 1e) can ensure uniform and stable deformation.

In metallic material systems, there exists a class of secondary hardening materials such as shape-memory alloys (SMAs, TiNi-based, Cu-based, Fe-based, etc.),<sup>16–18</sup> which can occur unique atom lattice shearing transformation rather than common dislocation glide, for example, stress-induced martensite phase transformation or martensite orientation deformation.<sup>19,20</sup> Figure S1 (Supporting Information) shows the tensile stress–strain curve of a commercial martensitic NiTi alloy and the corresponding deformation mechanisms. Upon loading, the NiTi alloy undergoes initial elastic deformation (stage I) before yielding over a stress plateau

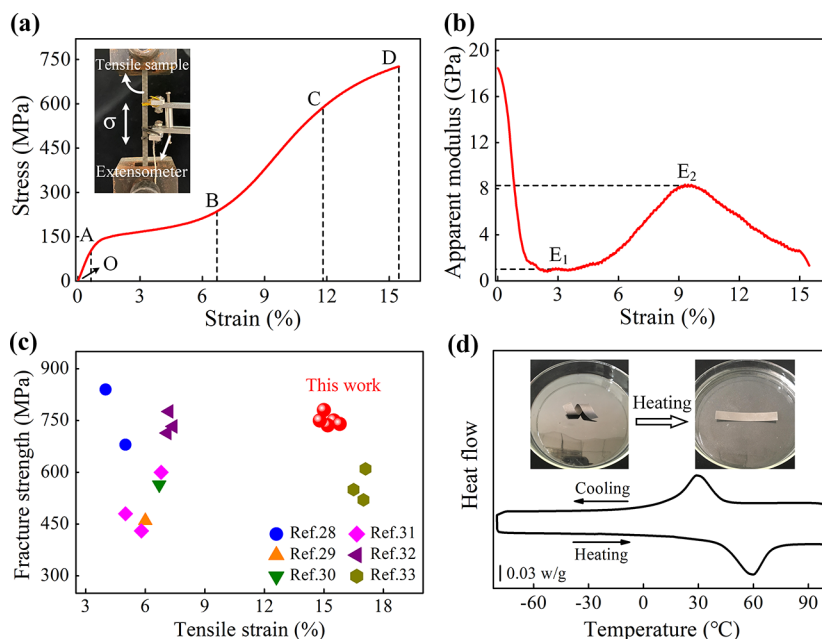


**Figure 2.** Mechanical properties and phase-transformation behavior of 3D-printed NiTi alloy bulk material. (a) Tensile stress–strain curve of the 3D-printed NiTi bulk sample. Inset is the real photo of tensile sample. (b) Evolution of apparent modulus versus strain of (a).  $E_1$  represents the low apparent modulus after yielding, and  $E_2$  represents the high apparent modulus after yielding. (c) Comparison of the fracture strength and tensile strain obtained from the alloys in this work and other LPBF-fabricated NiTi alloys. (d) DSC curve of 3D-printed NiTi alloy. The insets show the superior shape-recovery function of 3D-printed NiTi sheet upon heating.

with low stiffness via martensite variant reorientation (stage II), followed by a significant stiffening stage with rapidly increasing stress (stage III). What's more, this martensite transformation is fully reversible and can provide a great possibility for the architected metallic materials to display an excellent shape-recovery function. Although SMAs have been known for the shape-memory effect, few studies have considered applying this secondary hardening effect (self-hardening capacity) on macro-architected materials. Here we abandoned sophisticated or complex structural design and rather adopted the special deformation behavior of the constituent material. Hence, this strategy may apply to most conventional structures. This work will provide a simple but effective strategy for conventional metallic structures to realize uniform and stable deformation without localized deformation bands and strength collapse. To substantiate the effectiveness of our material deformation design strategy, we selected NiTi alloy as the probative constituent material and adopted laser powder bed fusion (LPBF) additive manufacturing (3D printing) to prepare various NiTi architected materials with different geometric structures.

## 2. EXPERIMENTAL DETAILS

An Eplus M100-T machine equipped with a maximum 200 W Yb-fiber laser beam with a 70  $\mu\text{m}$  diameter was used. The used process parameters of LPBF are laser power of 120 W, scanning speed of 500 mm/s, powder bed layer thickness of 30  $\mu\text{m}$ , and hatch spacing of 80  $\mu\text{m}$ . A scanning pattern of stripe rotation was used (see Figure S2).<sup>21</sup> Commercialized gas-atomized Ti–50.6 atom %Ni prealloy powders with particles of 15–53  $\mu\text{m}$  were used to build NiTi architectures on a NiTi substrate maintained at 180 °C. Lath samples with dimensions of 80  $\times$  12  $\times$  2 mm<sup>3</sup> were printed flat on the substrate and then cut into a thin sheet with dimensions of 80  $\times$  2  $\times$  0.8 mm<sup>3</sup> for tensile testing. The tensile direction is vertical to the building direction. The detailed sampling method is shown in Figure S3. Detailed information

on the machined rolled NiTi sheet sample is shown in the legend of Figure S1.

As contrast samples, the honeycomb structures made of a conventional metallic material of 6061 aluminum alloy were fabricated via wire–electrode discharge cutting. Another contrast sample of 3D-printed Al–Si10–Mg honeycomb architecture was fabricated through LPBF. The particle sizes of used commercial Al–Si10–Mg powders are 15–53  $\mu\text{m}$ . The process parameters are a laser power of 350 W, scanning speed of 1300 mm/s, powder bed layer thickness of 30  $\mu\text{m}$ , and hatch spacing of 180  $\mu\text{m}$ . The scanning pattern was the same as that for the 3D-printed NiTi alloy. The 3D-printed Al–Si10–Mg honeycomb samples were heat-treated at 380 °C for 2 h before testing to improve the ductility. All structures were modeled by the software SolidWorks. The wall thickness or stem diameter was 0.4 mm.

Tension and compression tests were conducted at 25 °C using a KQL universal testing machine. The tensile strain rate was  $5 \times 10^{-3} \text{ s}^{-1}$ . An extensometer with a gauge length of 25 mm was used during tensile testing. All 3D-printed NiTi specimens were cooled below 0 °C prior to deformation testing to ensure the martensitic state. At least three specimens were tested for each condition to ensure experimental reliability. All compression and shape-recovery processes were recorded with a video. The sample for characterizing the phase-transformation behavior was cut from tensile lath with a weight of 20 mg. The phase-transformation behavior was investigated using a TA Instruments Q20 DSC instrument at a heating/cooling rate of 5 °C min<sup>-1</sup>. Cubic sample with size of 10  $\times$  10  $\times$  10 mm<sup>3</sup> was printed for characterizing phase component. The phase component of 3D-printed NiTi alloy was characterized by X-ray diffraction using Bruker D8 Focus with Cu K $\alpha$  radiation. Digital image correlation (DIC, Mercury RT series) tests were conducted to reveal the local strain evolution of the honeycomb samples during compression. The error of the calculated volume fraction of local strain is <2%.

FEM simulation was carried out to analyze the local strain distribution of NiTi/Al honeycomb samples during compression. Patran/LS-DYNA was employed. We chose the single surface general contact to avoid the penetration phenomenon, and all surfaces were automatically contacted. To ensure the accuracy, the element edge length was 0.88 mm and there were 11 076 elements in total. The element type was Belytschko–Tsay shell element, which was fast,

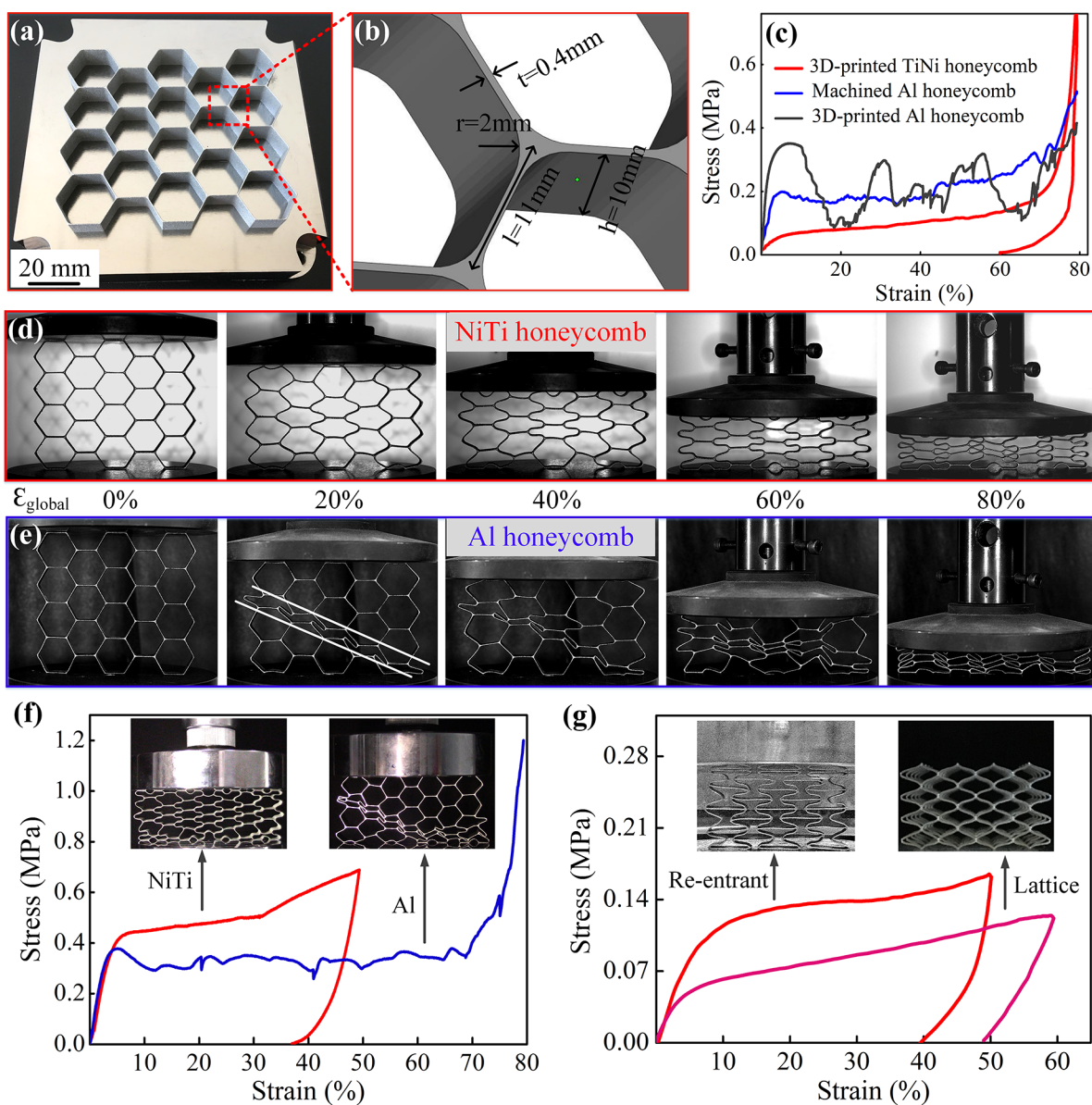


**Figure 3.** Compression tests of the architected metallic materials constructed of different constituent materials and different structures. (a) 3D-printed TiNi honeycomb structure. (b) Detailed structure parameters of the honeycomb shown in (a). (c) Compression stress–strain curves of a 3D-printed NiTi honeycomb sample ( $5 \times 4$  cells, the red curve), 3D-printed Al honeycomb sample (the blue curve), and machined Al honeycomb sample (the black curve). (d) Snapshots of the 3D-printed NiTi honeycomb sample at different global strains during compression. (e) Snapshots of the machined Al honeycomb sample at different global strains during compression. The parallel white lines at  $\epsilon_{\text{global}} = 20\%$  mark the localized deformation band. The strain values in the middle apply to both (d) and (e). (f) Compression comparison of the honeycomb samples with  $7 \times 5$  cells constructed of NiTi alloy and Al alloy. The former exhibits uniform and stable deformation, while the latter exhibits unstable deformation with the collapse of strength and emergence of local bands. (g) Compression tests of NiTi negative Poisson ratio structure and three-dimensional octahedral lattice structure, with both exhibiting uniform and stable deformation.

stable and efficient in large deformation problem by using “in-plane single point integral”. The model was between two rigid walls. The bottom wall was static, and the top wall moved at  $v = 0.3 \text{ m s}^{-1}$  to provide the pressure. The material attributes of the NiTi/Al model were obtained from the tensile stress–strain curves. For NiTi, the density  $\rho = 6.45 \times 10^{-9} \text{ t mm}^{-3}$ , the elastic modulus  $E = 18\,002.335 \text{ MPa}$ , the Poisson ratio  $\nu = 0.3$ , the yield stress  $\sigma_Y = 132.365 \text{ MPa}$ . For Al, the density  $\rho = 2.75 \times 10^{-9} \text{ t mm}^{-3}$ , the elastic modulus  $E = 39\,212.855 \text{ MPa}$ , the Poisson ratio  $\nu = 0.3$ , the yield stress  $\sigma_Y = 179.498 \text{ MPa}$ . The friction coefficient between the model and the walls was set as 0.17.

### 3. RESULTS AND DISCUSSION

First, considering from the unique manufacturing characters of LPBF, which exhibits local melting of metal powders followed by rapid solidification that is not exist in conventional smelting method,<sup>22–25</sup> we conducted characterization of the mechanical behavior of the 3D-printed NiTi alloy to verify if it is coincided with the designed deformation behavior. Figure 2 shows the mechanical properties and phase-transformation behavior of the 3D-printed NiTi alloy bulk material. Figure 2a shows the tensile stress–strain curve of a 3D-printed NiTi bulk sample. The inset shows a photograph of the tensile sample. It is obvious that the 3D-printed NiTi exhibits similar mechanical

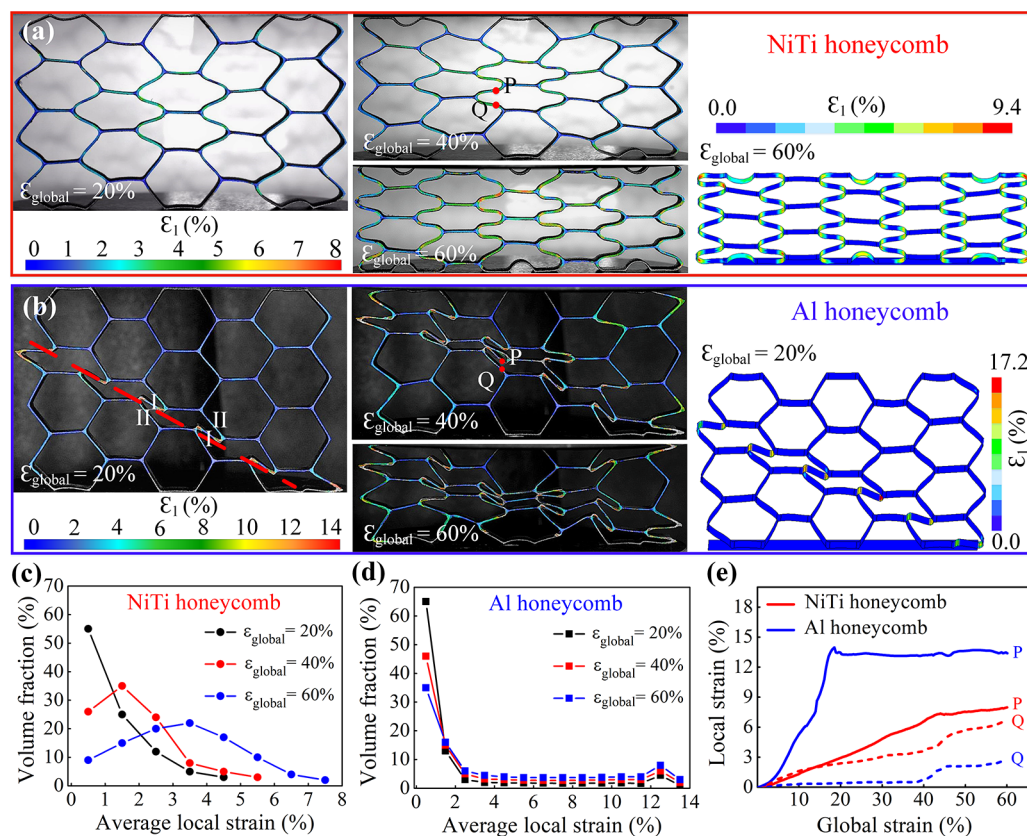


**Figure 4.** Digital image correlation analysis and FEM simulations of the local strain distribution within the 3D-printed NiTi honeycomb sample and machined Al honeycomb sample during compression. (a) Maximum principal strain maps of the NiTi honeycomb sample at different global strains obtained by the DIC and FEM. (b) Maximum principal strain maps of the Al honeycomb sample at different global strains obtained by the DIC and FEM. The red dashed line represents the localized deformation band. (c) Evolution of the local strain distribution of the NiTi honeycomb sample during compression. (d) Evolution of the local strain distribution of the Al honeycomb sample during compression. (e) Evolutions of the local strain of P and Q regions lying in the middle unit cell of the NiTi honeycomb and Al honeycomb during compression. These two regions are marked in the same location in the NiTi and Al honeycombs at  $\epsilon_{\text{global}} = 40\%$ . The P region represents the preferentially deformed region, and the Q region represents the latter deformed region.

behavior with the secondary hardening effect as described in Figure 1e. The corresponding apparent modulus evolution is shown in Figure 2b, which includes both a low modulus ( $E_1 \approx 1$  GPa) and a following high modulus ( $E_2 \approx 8$  GPa) after yielding, consistent with the designed material characteristics. X-ray diffraction (XRD) analysis indicated that the sample was in a fully B19' martensite state at room temperature (RT  $\approx 25$  °C) (Figure S4). Hence, it is speculated that the 3D-printed NiTi sample experienced four typical deformation stages during tensile loading (see Figure 2a) as commonly observed in conventionally fabricated NiTi in the martensite state,<sup>26,27</sup> including the initial elastic deformation of the martensite (O–A), the reorientation deformation of the martensite over a stress plateau (A–B), the elastic deformation of the oriented martensite (B–C), and the plastic deformation of the oriented martensite (C–D).

Figure 2c shows a comparison of the tensile fracture strengths and strains of the NiTi alloy material fabricated via LPBF. Compared with other reports,<sup>28–33</sup> the 3D-printed NiTi prepared in this work exhibited both a high fracture strength of  $750 \pm 30$  MPa and a large tensile fracture strain of  $15.5 \pm 0.5\%$ , reaching an excellent material property level combining both high strength and high ductility. These tensile properties are comparable with that of a conventional machined NiTi alloy (Figure S5), for which the tensile strain is 19% and the

fracture strength is 989 MPa. The high ductility will provide a guarantee for the large and nonfractured deformation capacity of the architected material. Figure 2d shows the differential scanning calorimetry (DSC) curve of the 3D-printed NiTi, revealing the reversible austenite–martensite transformation upon the cooling and heating process. The insets show that the 3D-printed sheet samples twisted at room temperature can almost completely recover to their original straight shape after heating. This result demonstrates the excellent shape-recovery property of the 3D-printed NiTi material.<sup>21,34</sup>

After that, we 3D-printed various architected metallic materials with different structures made of NiTi alloy to verify our proposed material deformation design strategy. As comparisons, similar structures constructed of conventional aluminum (Al) alloy were also fabricated with either LPBF or conventionally machining (cut from a bulk material via the wire–electrode discharge cutting method). The 3D-printed and machined aluminum alloy materials both presented typical elastic–plastic deformation behavior (Figure S6). Figure 3 shows the compression tests of several architected metallic materials constructed of different constituent materials and different geometric structures. Figure 3a is a photograph of the 3D-printed TiNi honeycomb sample with  $5 \times 4$  hexagonal cells. The geometric details of the cell are shown in Figure 3b. The cell wall thickness is  $400 \mu\text{m}$ , the side length is 11 mm, the

height in the building direction is 10 mm, and the hexagonal chamfer radius is 2 mm. Figure 3c shows the in-plane compression stress–strain curves of the 3D-printed NiTi honeycomb sample ( $5 \times 4$  cells, red curve) and also compares samples including a machined Al honeycomb (blue curve) and a 3D-printed Al honeycomb (black curve). It is apparent that the 3D-printed NiTi honeycomb experienced stable compression behavior up to 80% of the global strain without a decrease in mechanical strength. In comparison, the machined Al honeycomb sample showed obvious multistage weakening after an initial yield at  $\epsilon_{\text{global}} \approx 5\%$ . This loss of mechanical strength was even worse for the 3D-printed Al honeycomb sample, with a strength loss of  $>70\%$  after the initial yielding at  $\epsilon_{\text{global}} \approx 8\%$ . This comparison demonstrates the effectiveness of the designed deformation behavior of the constituent material in establishing stable deformation with a smooth stress–strain curve of the architected metallic materials.

Figure 3d shows a series of video snapshots of the 3D-printed NiTi honeycomb at different global strains during the compression test. It is clear that the deformation was largely uniform, and no local bands with excessive deformation were formed nor local fractures occurred, demonstrating a high damage tolerance. Video S1 (Supporting Information) provides a full recording of the compression process. Figure 3e presents a series of video snapshots of the machined Al honeycomb sample at different stages during compression. The global strain values shown between parts d and e are applied to both samples. It is evident that the Al honeycomb developed a severe local deformation band before reaching  $\epsilon_{\text{global}} = 20\%$  (marked with a parallel white line), while other cells outside the band experienced very limited deformation. The emergence of the local band corresponded to the first decrease of strength in the stress–strain curve in Figure 3c (blue curve). This unstable deformation behavior was even worse for the 3D-printed Al honeycomb sample, which suffered severe brittle fracture in the local bands and a sharp drop of mechanical strength (see Figure S7 and Figure 3c (black line)).

In addition, we also explored the mechanical behavior of architected NiTi/Al honeycombs with more unit cells of  $7 \times 5$  cells and  $9 \times 7$  cells. Figure 3f shows the compression stress–strain curves and deformation snapshots of NiTi honeycomb and Al honeycomb configured with  $7 \times 5$  unit cells, and the compression results of NiTi and Al honeycombs with  $9 \times 7$  cells are shown in Figures S8 and S9, respectively. It is evident that the NiTi multicell honeycombs ( $7 \times 5$  cells and  $9 \times 7$  cells) both displayed stable and uniform deformation behavior, as did the NiTi honeycomb with  $5 \times 4$  cells, without the emergence of local bands and collapse of strength. As a contrast, the Al multicell honeycombs ( $7 \times 5$  cells and  $9 \times 7$  cells) displayed severe localized deformation bands and loss of strength (see Figure 3f and Figure S9). Furthermore, NiTi architected materials with a negative Poisson ratio structure and a three-dimensional lattice structure also presented a stably increasing stress and uniform structure deformation without local bands (Figure 3g). These results further demonstrate the universality and applicability of this material deformation design on establishing the mechanical stability of architected metallic materials with various structures.

To clarify the mechanism of this specially designed constituent material deformation behavior for obtaining the mechanical stability of the architected metallic materials, we chose the relatively simple hexagonal honeycomb architecture as an example to make a deep exploration. Figure 4 shows the

real-time local strain evolution and distribution of architected NiTi/Al honeycombs ( $5 \times 4$  cells) via the digital-image correlation (DIC) technique and the finite-element method (FEM). The simulated deformation behavior and stress–strain curves are shown in Figure S10, and the simulation results generally match the experimental results. Figure 4a shows the maximum principal strain maps of the NiTi honeycomb at  $\epsilon_{\text{global}} = 20\%$ , 40%, and 60% obtained by the DIC and the strain map at  $\epsilon_{\text{global}} = 60\%$  obtained by the FEM. Figure 4b shows the same DIC maps for the Al honeycomb and the strain map at  $\epsilon_{\text{global}} = 20\%$  obtained by the FEM. It is apparent that the distribution and value level of local strain obtained by the DIC and FEM are similar at the same global strain. From these local strain maps, we can see that the NiTi honeycomb always exhibited a uniform strain distribution under whatever global strain, and different hexagon cells showed almost the same strain distribution and value. However, the Al honeycomb exhibited severely uneven strain distribution and high strain concentrations. The strain value of the cells lying in the local band reached up to 17.2%, while the other cells suffered almost zero strain.

The volume fraction of the region with a given average local strain was calculated from the DIC strain map, and the strain interval was set as 1%. Parts c and d of Figure 4 show the volume fraction distributions of the local strain at three global strain levels for the NiTi and Al honeycomb samples, respectively. During the whole deformation process, the NiTi honeycomb sample showed just one local strain peak. As the global strain increased, the local strain peak broadened, flattened, spread out, and shifted to higher strain ranges, demonstrating a typical continuous local strain distribution without any strain bifurcation in the structure. In contrast, the local strain distribution of the Al honeycomb sample exhibited two narrow peaks at all three global strain levels. The first peak represented the majority of the sample with little deformation and exhibited local strains within the range of 0–2%. The second peak represented a small volume fraction of the sample with large deformation and exhibited much higher strains of 12–13%. The maximum local strain was  $\sim 14\%$ , which was much higher than that for the NiTi honeycomb sample ( $\sim 8\%$ ). This bimodal local strain distribution reflected typical localized deformation behavior.

The preferentially deformed region “P” and latter deformed region “Q” in the middle hexagon cell of the two honeycombs were monitored and traced to obtain the evolution of local strain during the compression. Figure 4e shows the local strains of the P and Q regions versus the global strain. It is evident that the local strains of the P and Q regions in the NiTi honeycomb increased slowly and almost synchronously with the increase of global strain. The largest local strain of P was just  $\sim 8\%$ , and the strain difference between P and Q was  $<3\%$ , demonstrating that there existed no excessive deformation and no severe nonuniform deformation in the NiTi honeycomb. The gentle increase of local strain in the P region after  $\epsilon_{\text{global}} = 40\%$  was due to the self-strengthening property of the NiTi alloy with a high modulus deformation stage after yielding (B–C in Figure 2a). In this process, the further deformation of the preferentially yielded region was hindered, and other regions began dominating the whole deformation. So after  $\epsilon_{\text{global}} \approx 40\%$ , region Q deformed faster than region P. In the Al honeycomb, the local strain of region P increased rapidly to the largest value at  $\epsilon_{\text{global}} = 20\%$  and then remained changeless until the final value. However, region Q exhibited a local strain

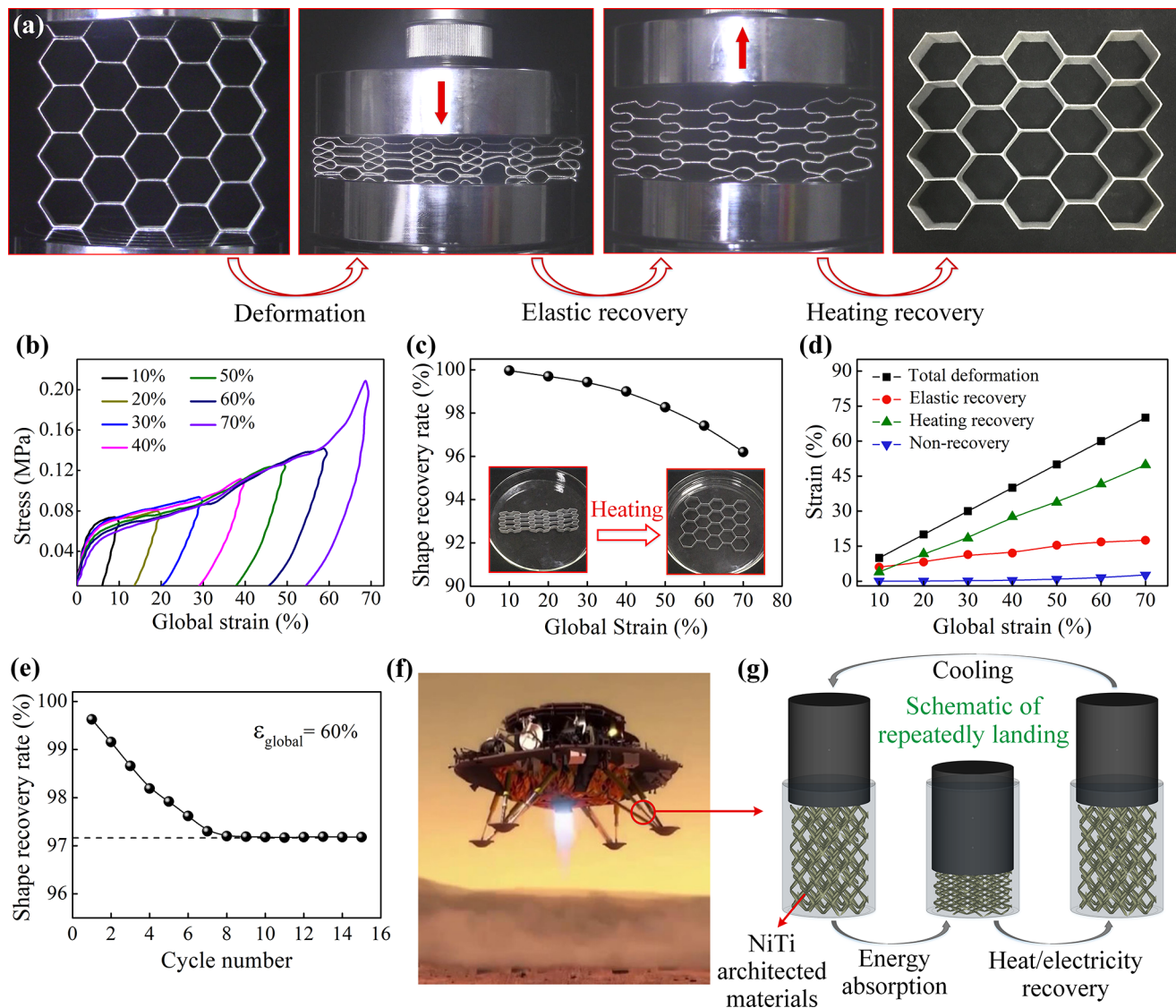


**Figure 5.** Shape self-recoverability of 3D-printed NiTi architected materials. (a) Pictures of a NiTi honeycomb sample before/after compression and after heating recovery. (b) Compression stress–strain curves of NiTi honeycomb in sequence from  $\epsilon_{\text{global}} = 10\%$  to  $\epsilon_{\text{global}} = 70\%$ . (c) Shape-recovery rate versus global strain. The insets show that the NiTi honeycomb compressed by 70% can almost completely recover to its initial shape after heating. (d) Percentages of different strain components as functions of the global strain. (e) Evolution of the shape-recovery rate under 15 deformation–recovery cycles at  $\epsilon_{\text{global}} = 60\%$ . (f) Lander photograph with multiple landing legs. Image reprinted from the Internet (<http://tv.cctv.com/cctvnews>). (g) Schematic of repeated landing of a landing leg when filled with NiTi architected materials as the energy-absorbing material.

smaller than 3% all the time. Such a huge strain difference between the P and Q regions demonstrated a severe nonuniform deformation in the Al honeycomb.

To further assess these two different deformation behaviors, we also conducted a statistical analysis of the distance variations between the upper and lower cell walls during compression and the curvature variations of one bent cell wall (shown in Figure S11). It is obvious that the Al honeycomb showed a larger distance deviation ( $\sim 14$  mm) among the different unit cells and a larger curvature ( $\text{max} = 120^\circ$ ) in a single cell wall than those of the NiTi honeycomb ( $\sim 5$  mm,  $\text{max} = 50^\circ$ ). This result suggested that the Al honeycomb experienced severe nonuniform deformation either in its overall structure or in a single unit cell and that the NiTi honeycomb suffered moderate and continuous deformation.

These distinctly different deformation behaviors of the NiTi and Al honeycomb architectures can be attributed to the

different stress–strain behaviors of the NiTi and aluminum alloy constituent materials. The initiation of the localized deformation band along the diagonal in the Al honeycomb sample is intrinsic and unavoidable because the diagonal plane is the mechanical maximum shearing stress plane when it suffers a uniaxial load. A hexagonal cell has three sides. The horizontal side does not respond to the compressive load in the vertical direction, and the two  $60^\circ$  sides experience the same bending force from the compressive load. Yielding via the bending of one  $60^\circ$  side will trigger the bending of the adjacent  $60^\circ$  side of the same orientation (group I) but strengthen the adjacent  $60^\circ$  side of the other orientation (group II), as indicated in Figure 4b. This self-guided propagation of local deformation leads to the formation of a deformation band along a diagonal line, as indicated by the parallel white lines in Figure 4b. For the NiTi honeycomb architecture, the rapid stiffening of NiTi (C–D in Figure 2a) via the elastic

deformation of the oriented martensite stops the initial local deformation and forces the deformation to spread to other regions of the architecture.<sup>35</sup> This leads to a stable and uniform compression process. In contrast, Al does not have this ability to stop local deformation due to its continuous low strain hardening state during plastic deformation (see A–B in Figure 1b), thus leading to the plastic collapse of the whole architecture.

Some consideration needs to be given to this designed stress–strain behavior. The strain span of the flow stress plateau should not be too small; otherwise, the local deformation is not sufficient to guarantee the large deformation of the whole structure. Additionally, the strain span cannot be too large; otherwise, the localized deformation band will form before the arrest effect is triggered. As seen in Figure 4d, the average local strain (for this sample) within the localized deformation band is 12–13%. Thus, the low modulus deformation stage of the constituent material must be below this strain level, for example, at 6–7%. Apparently, this threshold of the local strain level for the formation of a localized deformation band (12–13% in this case) is related to the structural attributes (cell thickness, geometry, architecture size, etc.). In this case, many other self-hardening metallic materials such as Fe-based SMAs may have their own strain threshold<sup>36</sup> and should be matched with suitable structural attributes. On the other side, this self-hardening capacity or strain span of the constituent material can also be tailored through material modification. For example, we can improve the apparent modulus of stage III (elastic deformation of the oriented martensite) of NiTi by increasing the dislocation density or hardening phase, thus enhancing the self-hardening capacity.<sup>37</sup> This regulation of the self-hardening capacity can accommodate more structural attributes and make this material deformation behavior apply to wider application requirements of architected metallic materials.

In addition, inherited from the superior shape-memory function of the constituent material, the 3D-printed NiTi architected materials also exhibited excellent shape self-recoverability. Figure 5a shows the pictures of the NiTi honeycomb architecture before/after compression deformation ( $\epsilon_{\text{global}} = 80\%$ ) and after heating recovery (shape-recovery rate  $>98\%$ ). Figure 5b shows a series of compression stress–strain curves of the NiTi honeycomb in sequence from  $\epsilon_{\text{global}} = 10\%$  to  $\epsilon_{\text{global}} = 70\%$ . After each deformation, the sample was heated to induce shape recovery. Figure 5c shows the shape-recovery rate versus the global strain. The insets show that the NiTi honeycomb compressed by 70% can almost completely recover to its original shape after heating. The full process is shown in Video S2 in the Supporting Information. The shape-recovery rate slowly decreased with the increasing global strain but was still  $>96\%$  when  $\epsilon_{\text{global}} = 70\%$ . Figure 5d plots the elastic recovery strain, heating recovery strain, and unrecoverable strain versus the global strains. The unrecoverable strain during compression is  $<3\%$ , demonstrating that the plastic deformation is small, thus indirectly reflecting the moderate and uniform deformation characteristics of the NiTi architected materials without high local strain concentration.

The cycle stability of shape recovery was also evaluated through 15 deformation–recovery cycles at  $\epsilon_{\text{global}} = 60\%$ . Figure 5e shows the evolution of the shape-recovery rate versus the cycle number. The shape-recovery rate (based on the original undeformed shape) decreased slightly from 99.7% to 97.2% during the previous eight deformation cycles and

remained constant thereafter, displaying the high cyclic stability of shape recovery. In addition, the NiTi re-entrant hexagonal structure and octahedral lattice structure also display high shape-recovery rates ( $>99.5\%$ ) after a large deformation (Figure S12). This combination of high damage tolerance, large nonfracture deformability, and superior shape self-recoverability gives the architected metallic materials unique advantages and huge potentials as reusable components in various applications, such as cushioning and energy-absorbing materials, intelligent self-driven robots, large displacement actuation devices and deployable structures, etc. It is worth mentioning that many other shape-memory alloys such as TiNi-based SMA (TiNiCu), Cu-based SMA (CuZnAl), Fe-based SMA (FeMnSi), etc. all may have similar mechanical and functional effects on the architected materials as the NiTi alloy does in this work. Additive manufacturing techniques would make these damage-tolerant functional architected metallic materials easily fabricated and have more possibility for practical applications.

A potential application scenario is the repetitive landings of the space lander, illustrated in Figure 5f and g. When the landing legs are filled with NiTi architected materials with cellular structure or lattice structure, these fillers can absorb energy when landing and then rapidly recover to the initial shape once stimulated via simple electricity or heating. After cooling, the NiTi architected materials recover to the martensite state and prepare for the next landing without replacing the fillers. The high cycle stability revealed in Figure 5e demonstrates that such energy-absorbing materials will have a longer service life and higher reliability. Hence, the adoption of NiTi architected materials can not only provide a stable, controllable, and predictable deformation manner but also offer reusable, economical, and lightweight energy-absorbing or driving materials.

## 4. CONCLUSIONS

In this work, a novel material deformation design strategy has been proposed to thoroughly solve the long-standing problem of mechanical instability in architected metallic materials. When loaded beyond the yield point, a rapid stiffening deformation stage with high apparent modulus is properly introduced in the constituent material to prevent the localized deformation band of architected metallic materials from evolving into excessive deformation and catastrophic collapse. The NiTi alloy was selected as a candidate constituent material, and the metallic 3D-printing technique of LPBF was adopted to prepare various architectures to substantiate this strategy. It is demonstrated that all of the architected metallic materials can exhibit a stable and uniform deformation behavior up to 80% of the global compression without emergence of local bands, collapse of strength, and structure damage. Besides the NiTi alloy, many other SMAs such as Cu-based SMA, Fe-based SMA, or secondary hardening metallic materials such as TRIP steel, TWIP steel, etc. may also have this unique self-strengthening deformation behavior and can be 3D-printed into arbitrary architectures. Specially, architected materials constructed of SMAs can display unprecedented shape recoverability in addition to damage-tolerant mechanical behavior. This work may bring new thoughts and methods to develop high-performance architected metallic materials with damage tolerance and functionality.

## ■ ASSOCIATED CONTENT

## SI Supporting Information

The Supporting Information is available free of charge at <https://pubs.acs.org/doi/10.1021/acsami.1c11226>.

Typical secondary hardening behavior of commercial NiTi SMA, stripe rotation scanning strategy used for 3D-printing, preparation procedure of 3D-printed NiTi tensile samples, XRD spectrum of 3D-printed NiTi alloy, comparison of the tensile properties of 3D-printed NiTi and machined NiTi alloy, tensile stress–strain curves of three different constituent materials, compression deformation behavior of the 3D-printed Al honeycomb, compression deformation behavior of the 3D-printed NiTi multicell honeycomb, compression deformation behavior of the machined Al honeycomb, finite element simulation results, deformation of the representative unit cell, and shape-recovery rates of the NiTi re-entrant negative Poisson ratio structure and octahedral lattice structure (PDF)

Compressive deformation comparison of 3D-printed NiTi honeycomb and machined Al honeycomb (MP4)

Shape recovery of a 3D-printed NiTi honeycomb upon heating (MP4)

## ■ AUTHOR INFORMATION

## Corresponding Authors

Shijie Hao – State Key Laboratory of Heavy Oil Processing, China University of Petroleum, Beijing 102249, P.R. China; [orcid.org/0000-0002-4427-851X](https://orcid.org/0000-0002-4427-851X); Email: [haoshijie@cup.edu.cn](mailto:haoshijie@cup.edu.cn)

Hong Yang – Department of Mechanical Engineering, The University of Western Australia, Crawley, Western Australia 6009, Australia; Email: [hong.yang@uwa.edu.au](mailto:hong.yang@uwa.edu.au)

Ying Yang – State Key Laboratory of Heavy Oil Processing, China University of Petroleum, Beijing 102249, P.R. China; Email: [yyang@edu.cn](mailto:yyang@edu.cn)

## Authors

Zhiwei Xiong – State Key Laboratory of Heavy Oil Processing, China University of Petroleum, Beijing 102249, P.R. China

Meng Li – Qian Xuesen Laboratory of Space Technology, China Academy of Space Technology, Beijing 100094, P. R. China

Yinong Liu – Department of Mechanical Engineering, The University of Western Australia, Crawley, Western Australia 6009, Australia; [orcid.org/0000-0002-8784-8543](https://orcid.org/0000-0002-8784-8543)

Lishan Cui – State Key Laboratory of Heavy Oil Processing, China University of Petroleum, Beijing 102249, P.R. China

Chengbo Cui – Qian Xuesen Laboratory of Space Technology, China Academy of Space Technology, Beijing 100094, P. R. China

Daqiang Jiang – State Key Laboratory of Heavy Oil Processing, China University of Petroleum, Beijing 102249, P.R. China; [orcid.org/0000-0003-4899-3868](https://orcid.org/0000-0003-4899-3868)

Hongshuai Lei – Institute of Advanced Structure Technology, Beijing Institute of Technology, Beijing 100081, P. R. China

Yihui Zhang – Department of Engineering Mechanics, Tsinghua University, Beijing 100084, P. R. China; [orcid.org/0000-0003-0885-2067](https://orcid.org/0000-0003-0885-2067)

Yang Ren – X-ray Science Division, Argonne National Laboratory, Argonne, Illinois 60439, United States; [orcid.org/0000-0001-9831-6035](https://orcid.org/0000-0001-9831-6035)

Xiaoyu Zhang – Beijing Institute of Spacecraft System Engineering, Beijing 100094, P. R. China

Ju Li – Department of Nuclear Science and Engineering and Department of Materials Science and Engineering, Massachusetts Institute of Technology, Cambridge, Massachusetts 02139, United States; [orcid.org/0000-0002-7841-8058](https://orcid.org/0000-0002-7841-8058)

Complete contact information is available at: <https://pubs.acs.org/doi/10.1021/acsami.1c11226>

## Author Contributions

Z.X. and M.L. contributed equally to this work. S.H., H.Y., and Y.Y. designed the project. Z.X. prepared the testing samples and conducted mechanical and functional experiments. M.L. and C.C. conducted the finite-element analysis of the structures. H.L., Y.Z., and X.Z. helped analyze the mechanics of the structures. Y.L., L.C., and J.L. modified and improved the theory and mechanism analysis. S.H., Y.L., L.C., H.Y., D.J., Y.Y., and Y.R. helped analyze the experimental data and revised the manuscript. All authors discussed the results and commented on the manuscript.

## Notes

The authors declare no competing financial interest.

## ■ ACKNOWLEDGMENTS

The authors acknowledge the financial support from the National Key R&D Program of China (2018YFB1105100), the NSFC (51971244 and 51731010), the Advanced Structural Technology Foundation of China (2020-JCJQ-JJ-024), and the Australian Research Council (DP180101744 and DP180101955).

## ■ REFERENCES

- (1) Gibson, L. J.; Ashby, M. F. *Cellular Solids: Structure and Properties*, 2nd ed.; Cambridge University Press: Cambridge, U.K., 1997.
- (2) Schaedler, T. A.; Carter, W. B. Architected Cellular Materials. *Annu. Rev. Mater. Res.* **2016**, *46* (1), 187–210.
- (3) Evans, A. G.; Hutchinson, J. W.; Ashby, M. F. Cellular Metals. *Curr. Opin. Solid State Mater. Sci.* **1998**, *3* (3), 288–303.
- (4) Pham, M. S.; Liu, C.; Todd, I.; Lertthanasarn, J. Damage-Tolerant Architected Materials Inspired by Crystal Microstructure. *Nature* **2019**, *565* (7739), 305–311.
- (5) Schaedler, T. A.; Jacobsen, A. J.; Torrents, A.; Sorensen, A. E.; Lian, J.; Greer, J. R.; Valdevit, L.; Carter, W. B. Ultralight Metallic Microlattices. *Science* **2011**, *334* (6058), 962–965.
- (6) Lakes, R. Foam Structures with a Negative Poisson's Ratio. *Science* **1987**, *235* (4792), 1038–1040.
- (7) Zheng, X.; Lee, H.; Weisgraber, T. H.; Shusteff, M.; DeOtte, J.; Duoss, E. B.; Kuntz, J. D.; Biener, M. M.; Ge, Q.; Jackson, J. A.; Kucheyev, S. O.; Fang, N. X.; Spadaccini, C. M. Ultralight, Ultrastiff Mechanical Metamaterials. *Science* **2014**, *344* (6190), 1373–1377.
- (8) Lee, J. Y.; An, J.; Chua, C. K. Fundamentals and Applications of 3D Printing for Novel Materials. *Appl. Mater. Today* **2017**, *7*, 120–133.
- (9) Trifale, N. T.; Nauman, E. A.; Yazawa, K. Systematic Generation, Analysis, and Characterization of 3D Micro-Architected Metamaterials. *ACS Appl. Mater. Interfaces* **2016**, *8* (51), 35534–35544.
- (10) Wang, D.; Xu, H.; Wang, J.; Jiang, C.; Zhu, X.; Ge, Q.; Gu, G. Design of 3D Printed Programmable Horseshoe Lattice Structures Based on a Phase-Evolution Model. *ACS Appl. Mater. Interfaces* **2020**, *12* (19), 22146–22156.
- (11) Mahmoudi, M.; Burlison, S. R.; Moreno, S.; Minary-Jolandan, M. Additive-Free and Support-Free 3D Printing of Thermosetting

Polymers with Isotropic Mechanical Properties. *ACS Appl. Mater. Interfaces* **2021**, *13* (4), 5529–5538.

(12) Klintworth, J. W.; Stronge, W. J. Elasto-plastic yield limits and deformation laws for transversely crushed honeycombs. *Int. J. Mech. Sci.* **1988**, *30* (3), 273–292.

(13) Papka, S. D.; Kyriakides, S. In-Plane Compressive Response and Crushing of Honeycomb. *J. Mech. Phys. Solids* **1994**, *42* (10), 1499–1532.

(14) Maskery, I.; Aboulkhair, N. T.; Aremu, A. O.; Tuck, C. J.; Ashcroft, I. A.; Wildman, R. D.; Hague, R. J. M. A Mechanical Property Evaluation of Graded Density Al-Si10-Mg Lattice Structures Manufactured by Selective Laser Melting. *Mater. Sci. Eng., A* **2016**, *670*, 264–274.

(15) Bonatti, C.; Mohr, D. Large Deformation Response of Additively-Manufactured FCC Metamaterials: From Octet Truss Lattices towards Continuous Shell Mesosstructures. *Int. J. Plast.* **2017**, *92*, 122–147.

(16) Ren, X.; Otsuka, K. Origin of Rubber-like Behaviour in Metal Alloys. *Nature* **1997**, *389* (6651), 579–582.

(17) Chluba, C.; Ge, W.; Lima de Miranda, R.; Strobel, J.; Kienle, L.; Quandt, E.; Wuttig, M. Ultralow-Fatigue Shape Memory Alloy Films. *Science* **2015**, *348* (6238), 1004–1007.

(18) Machado, L. G.; Lagoudas, D. C. *Introduction to Shape Memory Alloys*; Springer: Boston, 2008.

(19) Otsuka, K.; Ren, X. Physical Metallurgy of Ti-Ni-Based Shape Memory Alloys. *Prog. Mater. Sci.* **2005**, *50* (5), 511–678.

(20) Hao, S.; Liu, Y.; Ren, Y.; Jiang, D.; Yang, F.; Cong, D.; Wang, Y.; Cui, L. Achieving Superior Two-Way Actuation by the Stress-Coupling of Nanoribbons and Nanocrystalline Shape Memory Alloy. *ACS Appl. Mater. Interfaces* **2016**, *8* (25), 16310–16316.

(21) Xiong, Z.; Li, Z.; Sun, Z.; Hao, S.; Yang, Y.; Li, M.; Song, C.; Qiu, P.; Cui, L. Selective Laser Melting of NiTi Alloy with Superior Tensile Property and Shape Memory Effect. *J. Mater. Sci. Technol.* **2019**, *35* (10), 2238–2242.

(22) DebRoy, T.; Wei, H. L.; Zuback, J. S.; Mukherjee, T.; Elmer, J. W.; Milewski, J. O.; Beese, A. M.; Wilson-Heid, A.; De, A.; Zhang, W. Additive Manufacturing of Metallic Components – Process, Structure and Properties. *Prog. Mater. Sci.* **2018**, *92*, 112–224.

(23) Taheri Andani, M.; Bimber, B. A.; Amerinatanzi, A.; Shayesteh Moghaddam, N.; Hamilton, R. F.; Elahinia, M. Fabrication of NiTi through Additive Manufacturing: A Review. *Prog. Mater. Sci.* **2016**, *83*, 630–663.

(24) Kürsteiner, P.; Wilms, M. B.; Weisheit, A.; Gault, B.; Jäggle, E. A.; Raabe, D. High-Strength Damascus Steel by Additive Manufacturing. *Nature* **2020**, *582* (7813), 515–519.

(25) Hou, H.; Simsek, E.; Ma, T.; Johnson, N. S.; Qian, S.; Cissé, C.; Stasak, D.; Al Hasan, N.; Zhou, L.; Hwang, Y.; Radermacher, R.; Levitas, V. I.; Kramer, M. J.; Zaeem, M. A.; Stebner, A. P.; Ott, R. T.; Cui, J.; Takeuchi, I. Fatigue-Resistant High-Performance Elastocaloric Materials Made by Additive Manufacturing. *Science* **2019**, *366* (6469), 1116–1121.

(26) Liu, Y.; Liu, Y.; Van Humbeeck, J. Lüders-like deformation associated with martensite reorientation in NiTi. *Scr. Mater.* **1998**, *39* (8), 1047–1055.

(27) Kong, X.; Yang, Y.; Sun, Z.; Yang, H.; Liu, Y.; Ren, Y.; Cui, L.; Chen, C.; Hao, S. In-Situ High Energy X-Ray Diffraction Study of Microscopic Deformation Behavior of Martensite Variant Reorientation in NiTi Wire. *Appl. Mater. Today* **2021**, *22*, 100904.

(28) Bagheri, A.; Mahtabi, M. J.; Shamsaei, N. Fatigue Behavior and Cyclic Deformation of Additive Manufactured NiTi. *J. Mater. Process. Technol.* **2018**, *252*, 440–453.

(29) Yang, Y.; Zhan, J. B.; Sun, Z. Z.; Wang, H. L.; Lin, J. X.; Liu, Y. J.; Zhang, L. C. Evolution of Functional Properties Realized by Increasing Laser Scanning Speed for the Selective Laser Melting Fabricated NiTi Alloy. *J. Alloys Compd.* **2019**, *804*, 220–229.

(30) Yang, Y.; Zhan, J. B.; Li, B.; Lin, J. X.; Gao, J. J.; Zhang, Z. Q.; Ren, L.; Castany, P.; Gloriant, T. Laser Beam Energy Dependence of Martensitic Transformation in SLM Fabricated NiTi Shape Memory Alloy. *Materialia* **2019**, *6*, 100305.

(31) Shayesteh Moghaddam, N.; Saghaian, S. E.; Amerinatanzi, A.; Ibrahim, H.; Li, P.; Toker, G. P.; Karaca, H. E.; Elahinia, M. Anisotropic Tensile and Actuation Properties of NiTi Fabricated with Selective Laser Melting. *Mater. Sci. Eng., A* **2018**, *724*, 220–230.

(32) Lu, H. Z.; Yang, C.; Luo, X.; Ma, H. W.; Song, B.; Li, Y. Y.; Zhang, L. C. Ultrahigh-Performance TiNi Shape Memory Alloy by 4D Printing. *Mater. Sci. Eng., A* **2019**, *763*, 138166.

(33) Wang, X.; Yu, J.; Liu, J.; Chen, L.; Yang, Q.; Wei, H.; Sun, J.; Wang, Z.; Zhang, Z.; Zhao, G.; Van Humbeeck, J. Effect of Process Parameters on the Phase Transformation Behavior and Tensile Properties of NiTi Shape Memory Alloys Fabricated by Selective Laser Melting. *Addit. Manuf.* **2020**, *36*, 101545.

(34) Zhang, Q.; Hao, S.; Liu, Y.; Xiong, Z.; Guo, W.; Yang, Y.; Ren, Y.; Cui, L.; Ren, L.; Zhang, Z. The Microstructure of a Selective Laser Melting (SLM)-Fabricated NiTi Shape Memory Alloy with Superior Tensile Property and Shape Memory Recoverability. *Appl. Mater. Today* **2020**, *19*, 100547.

(35) Shariat, B. S.; Liu, Y.; Rio, G. Numerical Modelling of Pseudoelastic Behaviour of NiTi Porous Plates. *J. Intell. Mater. Syst. Struct.* **2014**, *25* (12), 1445–1455.

(36) Tanaka, Y.; Himuro, Y.; Kainuma, R.; Sutou, Y.; Omori, T.; Ishida, K. Ferrous Polycrystalline Shape-Memory Alloy Showing Huge Superelasticity. *Science* **2010**, *327* (5972), 1488–1490.

(37) Liu, Y.; Xiang, H. Apparent Modulus of Elasticity of Near-Equiatomic NiTi. *J. Alloys Compd.* **1998**, *270* (1–2), 154–159.

## Supporting Information

### **3D printing damage-tolerant architected metallic materials with shape recoverability via specially deformation design of constituent material**

*Zhiwei Xiong<sup>a†</sup>, Meng Li<sup>b†</sup>, Shijie Hao<sup>a\*</sup>, Yinong Liu<sup>c</sup>, Lishan Cui<sup>a</sup>, Hong Yang<sup>c\*</sup>, Chengbo Cui<sup>b</sup>, Daqiang Jiang<sup>a</sup>, Ying Yang<sup>a\*</sup>, Hongshuai Lei<sup>d</sup>, Yihui Zhang<sup>e</sup>, Yang Ren<sup>f</sup>, Xiaoyu Zhang<sup>g</sup>, and Ju Li<sup>h</sup>*

<sup>a</sup>State Key Laboratory of Heavy Oil Processing, China University of Petroleum, Beijing 102249, China

<sup>b</sup>Qian Xuesen Laboratory of Space Technology, China Academy of Space Technology, Beijing 100094, China

<sup>c</sup>Department of Mechanical Engineering, The University of Western Australia, Crawley, WA 6009, Australia

<sup>d</sup>Institute of Advanced Structure Technology, Beijing Institute of Technology, Beijing 100081, China

<sup>e</sup>Department of Engineering Mechanics, Tsinghua University, Beijing 100084, China

<sup>f</sup>X-ray Science Division, Argonne National Laboratory, Argonne, Illinois 60439, USA

<sup>g</sup>Beijing Institute of Spacecraft System Engineering, Beijing 100094, China

<sup>h</sup>Department of Nuclear Science and Engineering and Department of Materials Science and Engineering, MIT, Cambridge, MA 02139, USA

#### **Corresponding Author**

\*E-mail: haoshijie@cup.edu.cn (Shijie Hao)

\*E-mail: hong.yang@uwa.edu.au (Hong Yang.)

\*E-mail: yyang@.edu.cn (Ying Yang.)

#### **The PDF file includes:**

Figures S1 to S12

#### **Other supporting information for this manuscript includes:**

Movies S1 to S2

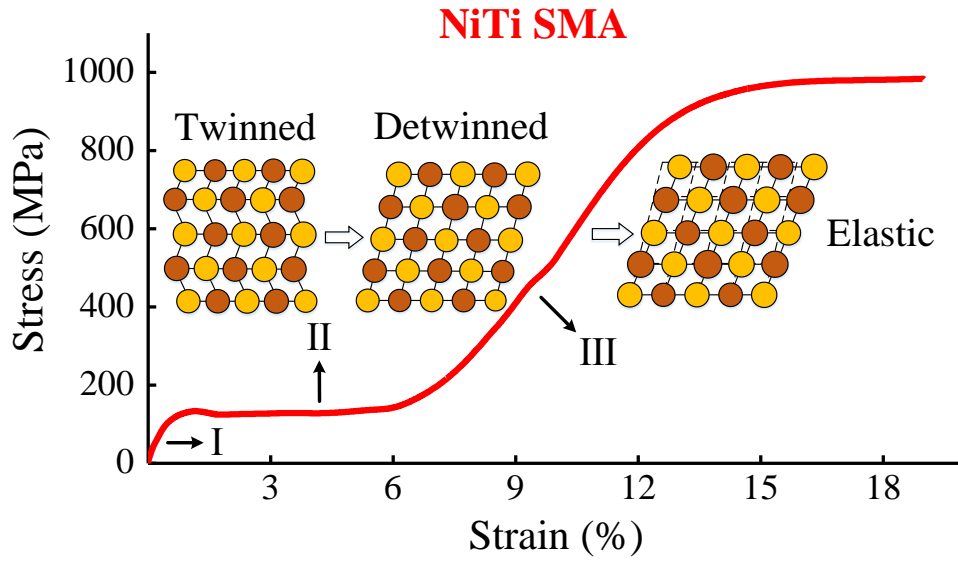


**Figure S1.** Tensile stress-strain curve of a commercial martensitic Ni<sub>50</sub>Ti<sub>50</sub> SMA sheet along the rolling direction and the corresponding deformation mechanism at atom level. The Ni<sub>50</sub>Ti<sub>50</sub> sheet was processed by smelting, cold-rolling and then cut into tensile sample. The sample underwent common annealing at 500 °C for 10 min. The testing temperature is room temperature (RT ~25 °C). The tensile strain rate was  $5 \times 10^{-3} \text{ s}^{-1}$ . The NiTi sheet displays obvious secondary hardening effect (stage III).

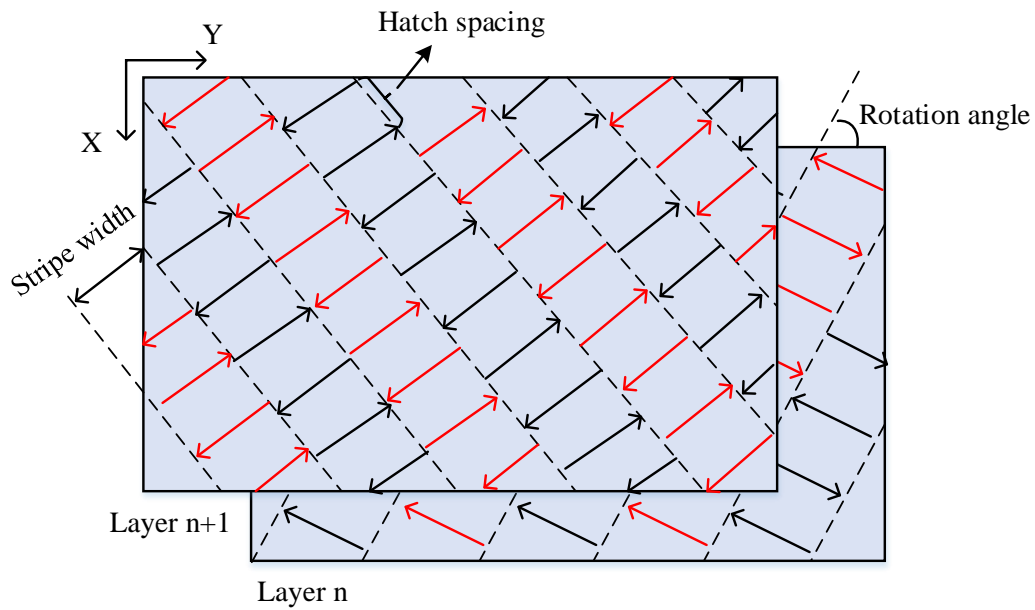


**Figure S2.** The stripe rotation scanning strategy used for the laser powder bed fusion fabrication. The stripe width was 4 mm, the rotation angle was  $67^\circ$ , and the hatch spacing was 0.08 mm. The laser will change direction for  $67^\circ$  at next layer. On a layer, the laser scans along special order: first in the regions with red arrows and then the regions with black arrows. This pattern is contributed to ensuring the whole layer heated evenly, decreasing thermal stress.

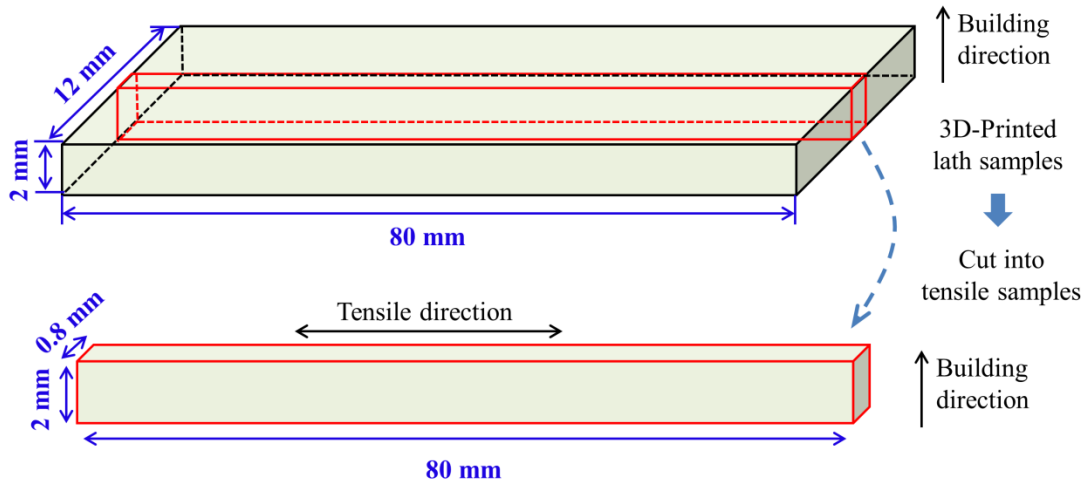


**Figure S3.** Detailed sample preparation procedure and size of 3D-printed NiTi alloy tensile samples. The 3D-printed lath samples were flat out on the substrate and would be cut into thin sheet via wire-electrode discharge cutting technique for tensile testing. The tensile direction is vertical to the building direction. An extensometer with gauge length of 25 mm was used during tensile testing.

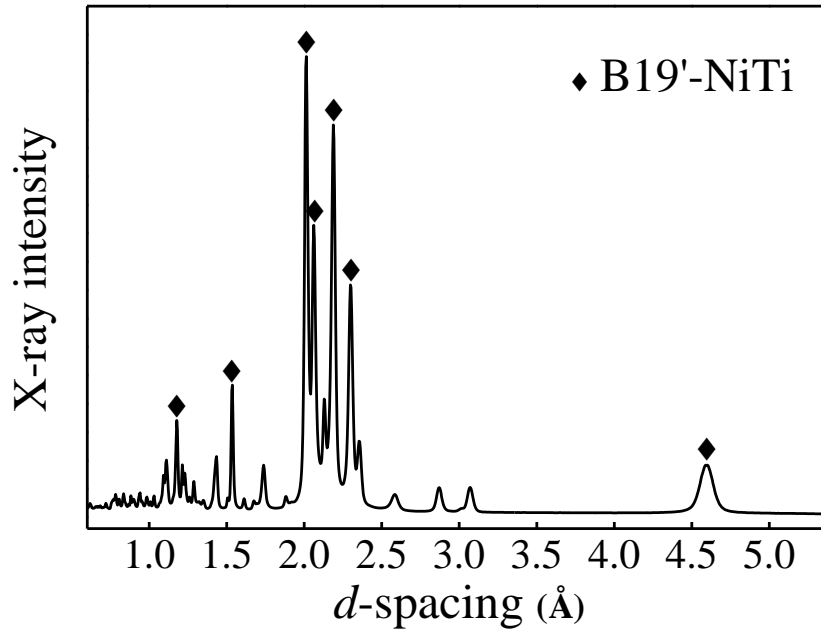


**Figure S4.** XRD spectrum of 3D-printed NiTi alloy at RT (~25 °C). All peaks are indexed to the B19' martensite phase, demonstrating there are mainly martensite phase in 3D-printed NiTi alloy. Due to the block sample and porous structures both adopt same process parameters; the porous structures in the following contents also have similar phase components.

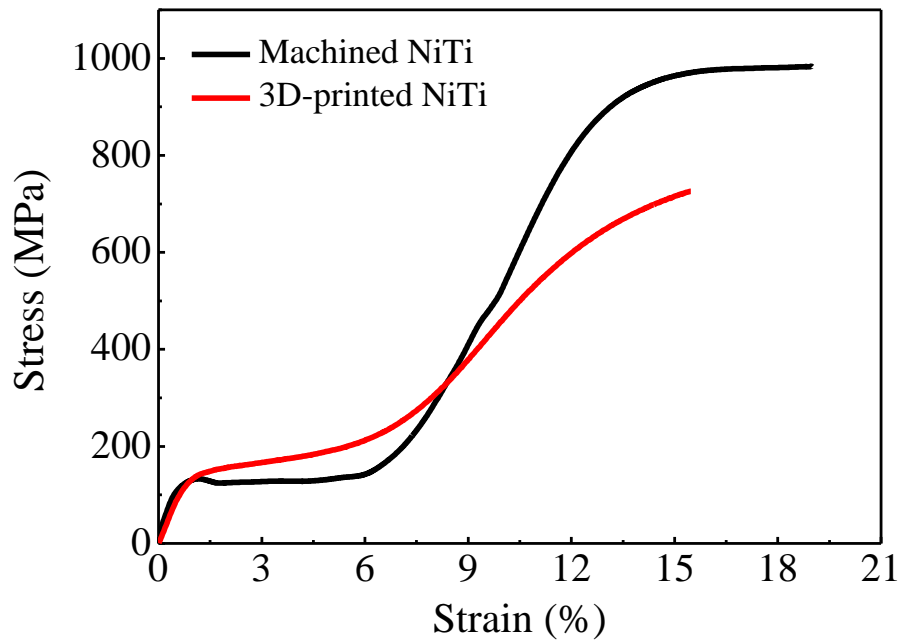
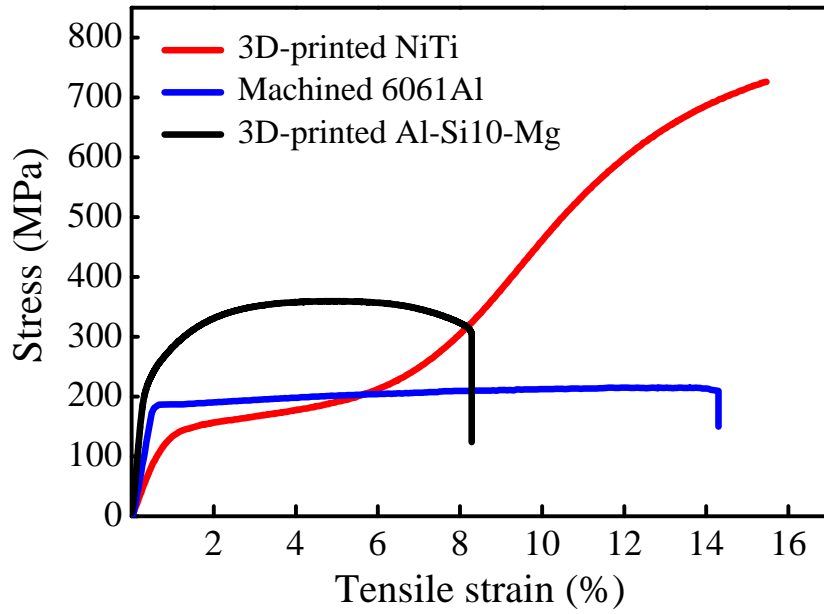


**Figure S5.** Tensile stress-strain curves of machined NiTi and 3D-printed NiTi. The curve of machined NiTi comes from Figure S1, which is obtained from conventional rolled Ni<sub>50</sub>Ti<sub>50</sub> sheet along the rolling direction. The machined NiTi exhibits tensile fracture strain of 19% and fracture strength of 989 MPa. It is found although the tensile fracture strength of 3D-printed NiTi is slightly lower than machined NiTi because of the coarse grain size; the tensile strain is comparable with that of machined NiTi.



Constituent material	Yield strength (MPa)	Elongation (%)
3D-printed NiTi	120-150	14-16
Machined 6061Al	170-200	12-15
3D-printed Al-Si10-Mg	220-250	7-9

**Figure S6.** Typical tensile stress-strain curves of three different constituent materials, including 3D-printed NiTi, 3D-printed Al-Si10-Mg and machined 6061 Al alloy, and the statistics for the yield strength and elongation. At least three tensile samples were tested at RT with a strain rate of  $10^{-3} \text{ s}^{-1}$ . The detailed fabricating method and parameters are listed in *Experimental details* in the manuscript.

### 3D-printed Al-Si10-Mg honeycomb

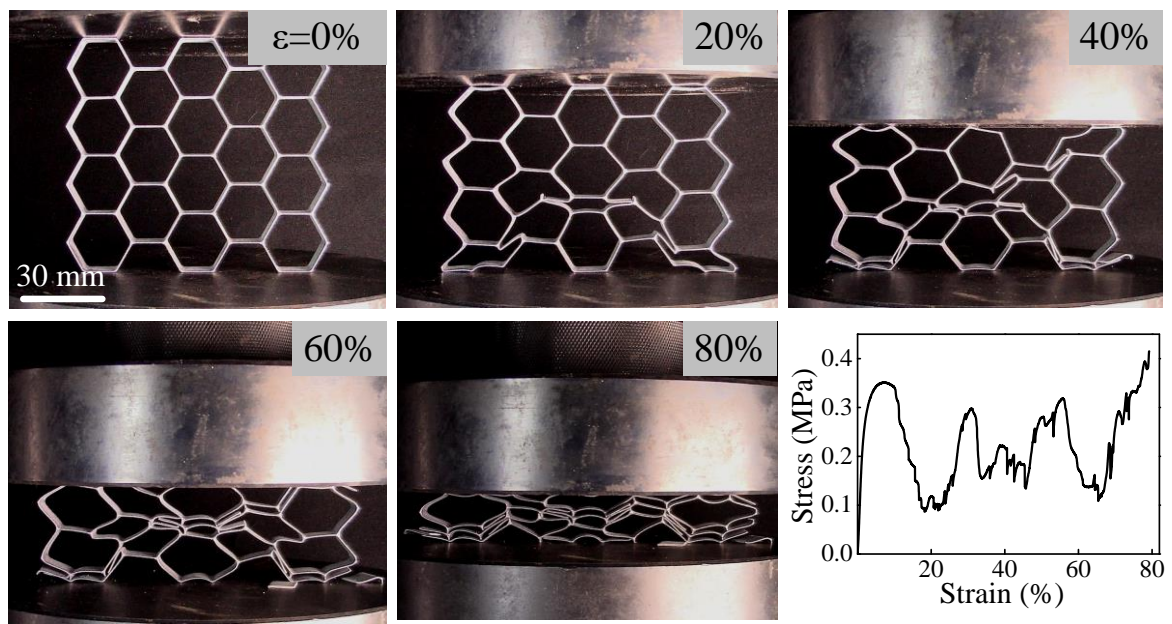
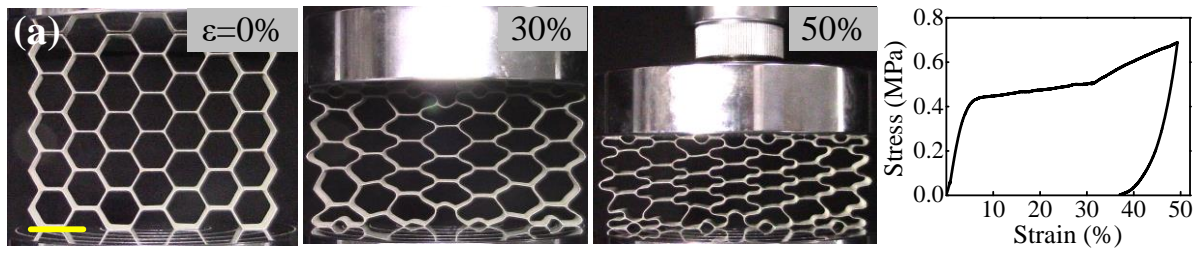


**Figure S7.** Compression deformation behaviour and stress-strain curve of the 3D-printed Al-Si10-Mg honeycomb sample. The sample exhibited fractured and collapsed deformation, accompanied by severe localized deformation bands and collapse of mechanical strength.

### NiTi honeycomb ( 7 × 5 cells)



### NiTi honeycomb ( 9 × 7 cells)

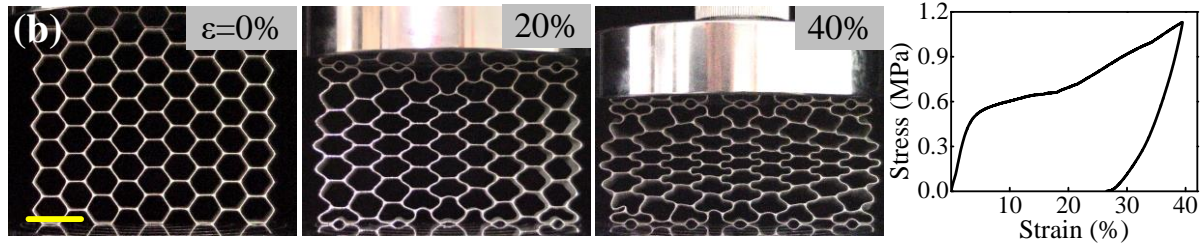
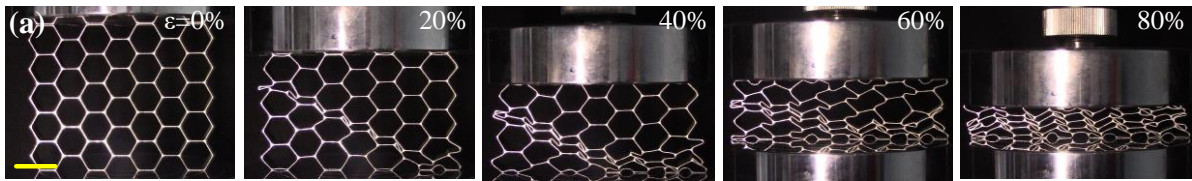


**Figure S8.** Compression deformation behaviour and stress-strain curves of 3D-printed NiTi multi-cell honeycomb samples. (a) Snapshots of a NiTi honeycomb sample with 7 × 5 cells at different global strains during compression and the corresponding stress-strain curve. (b) Snapshots of a NiTi honeycomb sample with 9 × 7 cells at different global strains during compression and the corresponding stress-strain. Both samples exhibited stable and uniform deformation behaviour without localized deformation bands of high strain or a collapse in mechanical strength. The scale bar is 25 mm.

Machined Al honeycomb (7×5 cells)



Machined Al honeycomb (9×7 cells)

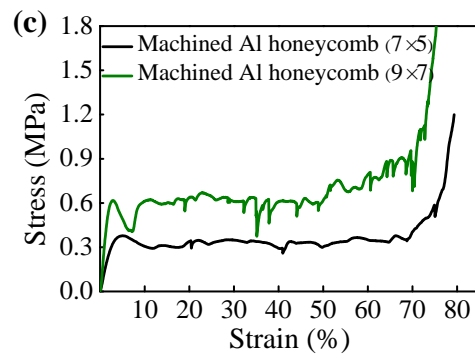
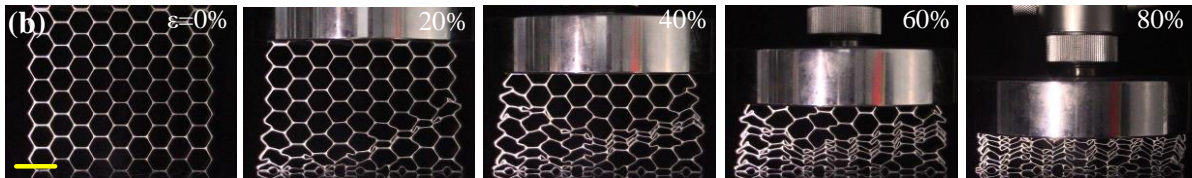


**Figure S9.** Compression deformation behaviour and stress-strain curves of machined 6061 Al alloy honeycomb architectures with more unit cells. (a) Snapshots of a machined 7×5 cells 6061 Al honeycomb sample at different compression strain. (b) Snapshots of a machined 9×7 cells 6061 Al honeycomb sample at different compression strain. (c) Compression stress-strain curves of the two samples displaying obvious catastrophic collapses of mechanical strength during compression. The scale bar is 25 mm.

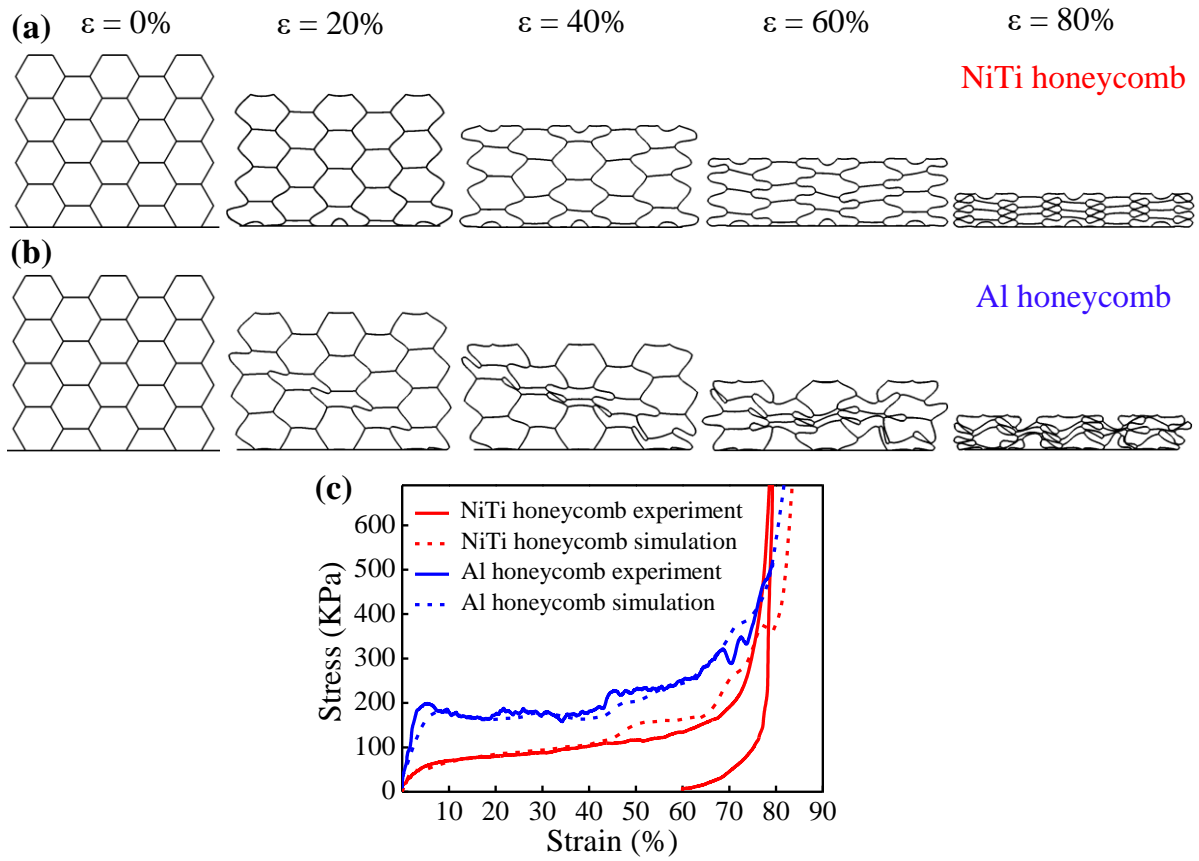


**Figure S10.** Finite element simulation results for the NiTi honeycomb and Al honeycomb. (a) The simulated deformation process of the NiTi honeycomb. (b) The simulated deformation process of the Al honeycomb. (c) The compression stress-strain curves of experiments and simulations. Both the structure deformation and stress-strain curves of the simulation are well-matched with the experimental results (Figures 3c and 3e), which verifies the reliability and rationality of simulation.

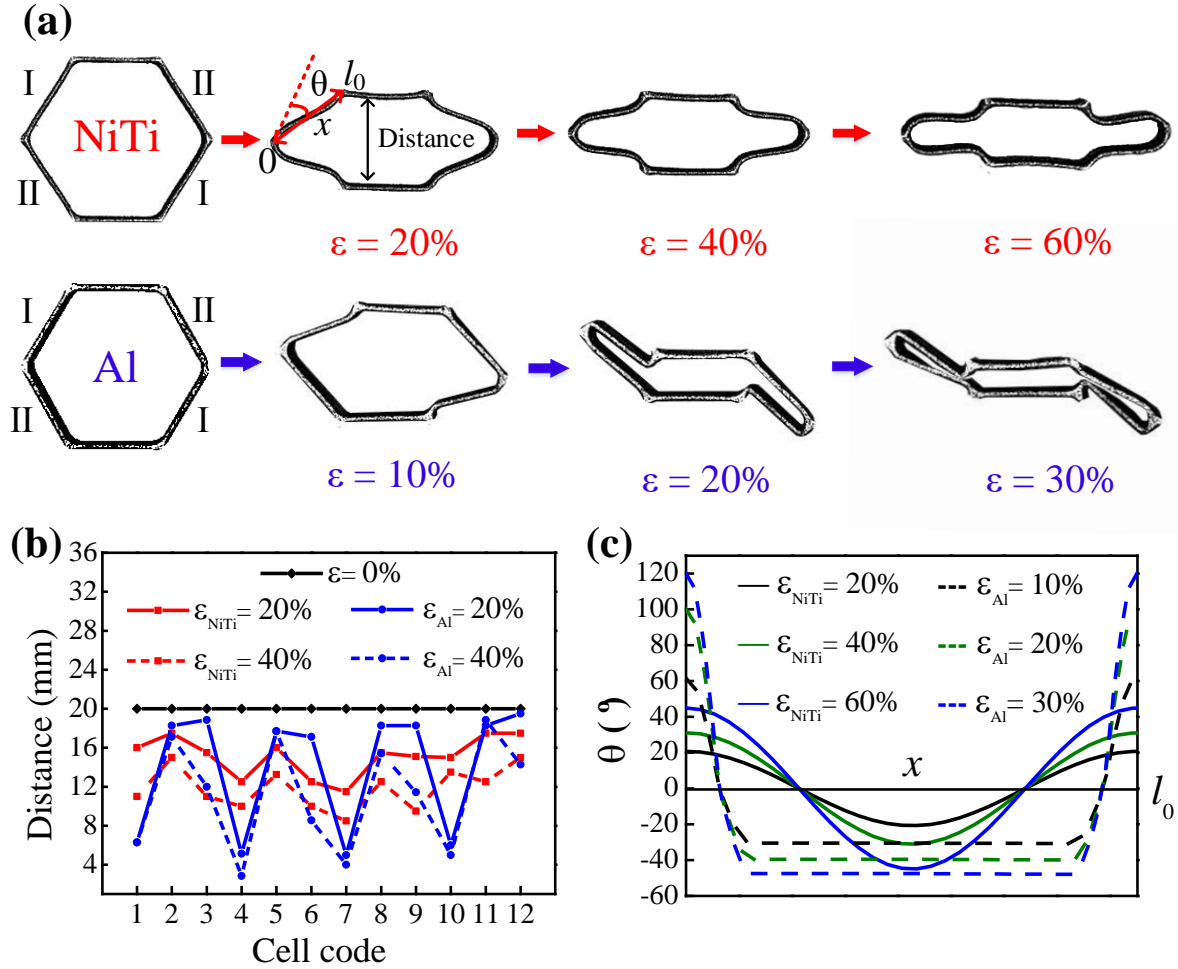


**Figure S11.** Deformation of a representative NiTi unit cell and Al unit cell during compression and corresponding distance and curvature evolution. (a) The shape transformation at different global strains. (b) The distance variations between upper and lower cell walls. All 12 unit cells of NiTi honeycomb and Al honeycomb were calculated at global strain of 0%, 20% and 40%, respectively. At the same global strain, the Al honeycomb presents larger deviation among 12 unit cells than that of the NiTi honeycomb, demonstrating severe uneven deformation. (c) The curvature ( $\theta$ ) versus distance ( $x$ ) in a group “I” cell wall. The curvature was defined by the angle  $\theta$  between the tangent line and connection line of two ends, whose length ( $l_0$ ) is the side length of a cell wall.  $x$  represents the distance from one end. It is obvious that the Al unit cell wall suffers larger bending deformation than NiTi unit cell, and the most deformation is concentrated on the two ends. In contrast, the NiTi unit cell wall shows moderate and continuous bending deformation.

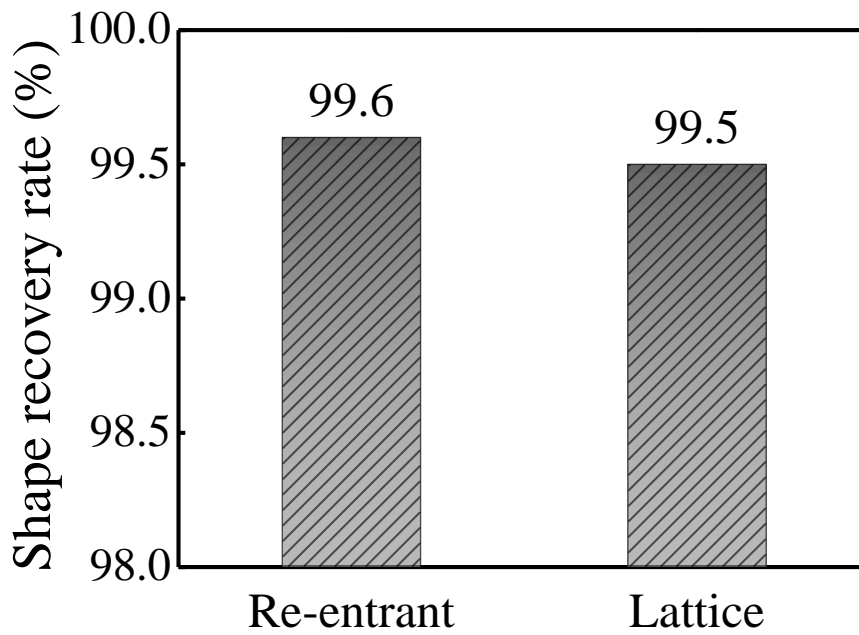


**Figure S12.** Shape recovery rates of the NiTi re-entrant negative Poisson ratio structure and octahedral lattice structure after heating, which are 99.6% and 99.5%, respectively, suggesting that both structures display excellent shape recovery function.

**Video S1.** Compressive deformation comparison of a 3D-printed NiTi honeycomb architecture and a machined Al honeycomb architecture.

**Video S2.** Shape recovery of a 3D-printed NiTi honeycomb architecture upon heating.